

The study of threshold behaviour of effective potential for ${}^6\text{Li}+{}^{58,64}\text{Ni}$ systems

M. Biswas^a, Subinit Roy^{a,1}, M. Sinha^a, M.K. Pradhan^a,
A. Mukherjee^a, P. Basu^a, H. Majumdar^a, K. Ramachandran^b,
A. Shrivastava^b

^a*Saha Institute of Nuclear Physics, I/AF Bidhan Nagar, Kolkata - 700064, India.*

^b*Nuclear Physics Division, Bhabha Atomic Research Centre, Mumbai-400085, India.*

Abstract

The elastic scattering for ${}^6\text{Li}+{}^{64}\text{Ni}$ system was measured in the bombarding energy range of $13 \text{ MeV} \leq E_{lab} \leq 26 \text{ MeV}$. A phenomenological optical model analysis was performed and the behaviour of the surface strengths of the potential components with decreasing energy was extracted. A further analysis of the measured angular distributions, along with the existing data for ${}^6\text{Li}+{}^{58}\text{Ni}$, was performed with two different model potentials - one with the folded potential normalized with a complex factor (OMP1) and the other with a *hybrid* potential composed of a renormalized folded real and a phenomenological imaginary (OMP2) potential components - were used in the calculation. All the model potentials predict similar energy dependent behaviour for the interaction potential around the barrier. The observed energy dependence of the strengths of the real and imaginary potentials corroborate with the dispersion relation prediction for both the ${}^6\text{Li}+{}^{64}\text{Ni}$ and ${}^6\text{Li}+{}^{58}\text{Ni}$ systems. Though the evidence of breakup is distinct in the energy variation of the potential strengths, close to the barrier the variation is more in the line of conventional threshold anomaly. Also the threshold behaviour of the interaction potential does not indicate any distinct isotopic dependence.

Key words: NUCLEAR REACTIONS ${}^{58}\text{Ni}$, ${}^{64}\text{Ni}({}^6\text{Li}, {}^6\text{Li})$, Coulomb barrier energies, measured $\sigma(\theta)$. Double folding model, threshold behaviour.

PACS: 25.70.Bc; 24.10.Ht; 27.20.+n

¹ Corresponding author. E-mail: subinit.roy@saha.ac.in

1 Introduction

Loosely bound nuclei are liable to breakup in a nuclear collision process. The breaking up of the nucleus can, subsequently, affect the other nuclear processes in a manner not observed in collisions involving only tightly bound nuclei. Extensive investigations, both experimentally and theoretically, are being pursued in recent years to understand the effect of breakup on elastic scattering [1,2,3,4,5,6,7]. One of the primary motivations is to probe the influence of break up process on the threshold behaviour of optical potential at near the Coulomb barrier energies.

The conventional threshold behaviour of the optical potential for tightly bound nuclei shows a rapid rise in the strength of the real potential in the vicinity of the Coulomb barrier with a sharp fall in the strength of the imaginary potential in the same energy range. It has been demonstrated that the coupling of relative motion to other reaction channels like inelastic excitations, transfers to the bound states contributes an attractive real polarization potential which in turn enhances the real strength at energies around the barrier [8,9]. The rapid decrease of fusion and other of the reaction processes with decreasing energy induces the sharp fall in the strength of the imaginary potential. The observed threshold behaviours of the potential components for the tightly bound nuclei are demonstrated to be connected by a dispersion relation, a manifestation of causality in nuclear collision process [9].

On the other hand, the dynamical effect of coupling to break up channels of weakly bound projectiles is to introduce a repulsive real polarization potential [10,11]. At above barrier energies the effect of breakup of the projectile was demonstrated through the reduction needed in the strength of the folded real potential describing the elastic scattering of projectiles like ${}^6,7\text{Li}$ and ${}^9\text{Be}$ [8]. With the bombarding energy decreasing for the scattering of ${}^6\text{Li}$ projectile (breakup threshold = 1.67 MeV) from heavy targets, the real potential strength exhibits a decline around the Coulomb barrier energy while the imaginary potential exhibits a rise in the surface strength [1,12]. Attempt has been made to understand this behaviour in terms of dispersion relation [12] and the observed threshold behaviour is termed as breakup threshold anomaly (BTA). For targets like ${}^{208}\text{Pb}$, due to strong Coulomb field, the breakup reaction channels do not close down rapidly near the barrier or at sub-barrier energies. Experimental observations suggest that the breakup cross section is even larger than the fusion cross section in the vicinity of the barrier [13,14,15,16]. As the coupling to breakup process contributes a repulsive dynamical polarization potential, the normal threshold anomaly (TA) in the real potential arising out of the attractive real polarization contribution of the conventional couplings, may disappear. The effective real potential strength may even show a declining trend with further decrease in energy if the breakup coupling

dominates over the conventional couplings at near barrier energies. Recently, So, *et al.* [17] have shown, based on the extended optical model approach, that the real and imaginary polarization potential components for scattering of ${}^6\text{Li}$ from ${}^{208}\text{Pb}$, when decomposed into direct and fusion contributions, satisfy the dispersion relation separately. The fusion part in this case showing a conventional threshold behaviour while the direct part exhibits a smooth and relatively weak energy dependence. For ${}^7\text{Li}$, a more strongly bound projectile (b.u. threshold = 2.43 MeV) compared to ${}^6\text{Li}$, the optical potential describing the scattering from heavy targets shows up a threshold behaviour like the strongly bound projectiles [1,18] and the energy variations of the real and imaginary components can be connected by the dispersion relation prediction.

Scattering of the weakly bound nuclei on lighter targets throws up a more complicated situation. The analyses of elastic scattering of ${}^{6,7}\text{Li}$ from ${}^{28}\text{Si}$ [7,19] show that both these projectiles, despite having different breakup threshold, exhibit similar trend in energy dependence of optical potential components. The imaginary potential for ${}^6\text{Li}+{}^{28}\text{Si}$ does not show the characteristic rise on approaching the barrier, rather it decreases after a small rise in strength just above the barrier. The real potential on the other hand is energy independent with a slight tendency to decrease as energy is decreased. Unlike the observations of scattering from lighter target nuclei, F.A. Souza, *et al.* [20] have found that the optical potential describing the elastic scattering of ${}^6\text{Li}$ and ${}^7\text{Li}$ from medium mass ${}^{59}\text{Co}$ exhibits a behaviour similar to that of the more tightly bound systems indicating the existence of a conventional threshold anomaly. However, as pointed out by the authors, looking at the energy dependence of the real and imaginary strengths of ${}^6\text{Li}+{}^{59}\text{Co}$ system carefully one can also categorize the threshold behaviour as breakup threshold anomaly (BTA). On approaching the barrier, the real strength shows a weak declining trend. The surface strength of the imaginary potential rises in the same energy region before falling again with decreasing energy. No attempt has been made to establish the dispersion relation connectivity between the observed behaviours. Further investigation of ${}^6\text{Li}$ scattering from medium mass targets is, therefore, necessary to identify the general behaviour of the interaction potential around the barrier. In general, for medium and light mass targets with reduced strength of the Coulomb field, the Coulomb induced breakup cross section is expected to decrease near the barrier. Thus the open question is how far the breakup of loosely bound projectiles, in the presence of conventional couplings, determines the threshold behaviour of interaction potentials for medium or light mass targets? The answer to this question will also address to the problem of target mass dependence of threshold anomaly for loosely bound projectiles.

We report, in this context, a systematic investigation of elastic scattering of ${}^6\text{Li}$ from ${}^{58,64}\text{Ni}$ targets at bombarding energies around the barrier. The isotopes of Ni have very similar deformation values, $\beta_2=0.17$ and 0.18 respectively for

^{58}Ni and ^{64}Ni . It was demonstrated by Keeley *et al.* [21] that both these isotopes exhibit similar threshold behaviour of potential for scattering with ^{16}O indicating that the threshold anomaly developed predominantly from inelastic couplings. We intend to investigate the energy dependence of the optical potential for the projectile ^6Li scattered from these two Ni isotopes. The primary interest is to see the manifestation of coupling to the continuum on the threshold behaviour of the interaction potential in the presence of strong inelastic couplings. The elastic scattering angular distributions for $^6\text{Li}+^{64}\text{Ni}$ have been measured at bombarding energies around the barrier to compare with the existing data of $^6\text{Li}+^{58}\text{Ni}$ [22]. The experimental details have been given in Section 2. The model calculation and the analysis have been presented in Section 3, followed by the results and discussion in Section 4.

2 Experimental Details

The experiment was carried out at 14UD TIFR/BARC Pelletron Facility in Mumbai, India. Self-supporting targets were prepared by electron gun evaporation technique from 99% enriched metallic ^{64}Ni isotope. Two different targets of thickness $61\mu\text{g}/\text{cm}^2$ and $376\mu\text{g}/\text{cm}^2$ respectively, were used for the experiment. The targets were bombarded with ^6Li beam from the pelletron at energies of 13, 14, 17, 19 and 26 MeV. The beam current during the experiment was varied from 1 to 7 pA. The current was measured using a Current Integrator, the output of which was fed into a CAMAC Scaler to obtain the integrated charge. The elastically scattered particles were detected with conventional telescope arrangement. Two silicon surface barrier detector telescopes were used in the two parts of the experiment. In the first part the telescopes were set with 25μ and 15μ thick ΔE detectors and 300μ thick E detectors to detect the scattered particles. In the second part the ΔE detectors of thickness 15μ and 10μ were used and these were followed by 3mm and 500μ E detectors respectively. The telescopes were placed on a rotatable arm at an angular separation of 10° . The solid angles subtended by the telescopes at the target centre were 0.076, 0.17, 0.06 and 0.11 msr respectively. The angular opening corresponding to these solid angle values were in the range of 0.5° to 0.8° . Two monitor detectors of thickness 3mm were mounted at $\pm 15^\circ$ about the beam axis, at a distance of 41.7cm in a 1m diameter scattering chamber. These two detectors were used to monitor the beam position and also for the purpose of normalization. Calibration runs were taken with a standard Bi target after each energy change. Using the Rutherford scattering between ^6Li and ^{209}Bi at these energies, the detector solid angles and the relative normalization between the telescopes were determined from the calibration runs. The statistical error in the data is less than 1% in the forward angles and a maximum of 16% in the backwards angles. The overall error in the data varied from

5% to 17%. The data were recorded using the Linux based data acquisition system LAMPS [23]. The measured elastic cross sections with respect to the Rutherford cross sections are shown in Fig.1 along with the model (see next section) calculations.

3 Analysis

Optical model (OM) analysis was carried out using three different model potentials. Firstly we performed the optical model analysis of our ${}^6\text{Li}+{}^{64}\text{Ni}$ data using the parametric Woods Saxon (WS) forms for both the real and imaginary potentials. Subsequently, the new data of ${}^6\text{Li}+{}^{64}\text{Ni}$ and the existing data of ${}^6\text{Li}+{}^{58}\text{Ni}$ [22] were further analysed with two other model potentials, namely, (i) the renormalized folded real and imaginary potentials, and (ii) a 'hybrid' potential consisting of a renormalized folded real and a parametric Woods Saxon imaginary components. The use of different model potentials was intended to make the extraction of energy dependence of the surface strengths of the potential components as much model independent as possible.

3.1 Phenomenological OM analysis of ${}^6\text{Li}+{}^{64}\text{Ni}$ data

The phenomenological optical model potential used to describe the elastic angular distributions at each energy had the following form

$$U_{OM}(R) = V(R; V_o, R_o, a_o) + i[W_F(R; W_o, R_w, a_w) + W_D(R; W_s, R_s, a_s)](1)$$

where $V(R)$ denotes the volume type WS real potential, $W_F(R)$ is a volume type WS imaginary potential to simulate the fusion after penetration of the barrier and $W_D(R)$ is a derivative type WS imaginary potential to account for the absorption due to reactions occurring at the surface.

The fitting procedure to obtain the parameters of the best fit potential can be summarized as follows. The search code ECIS94 [24] was used to perform the model calculations. The volume imaginary potential W_F was kept fixed for all the energies with the parameters set at $W_o=50.0$ MeV, $r_w=1.0$ fm and $a_w=0.25$ fm. At the highest energy, the real potential parameters for ${}^6\text{Li}+{}^{58}\text{Ni}$ from Ref.[22] were used as the starting parameters. Keeping the real radius fixed, searches were performed over the remaining five free parameters, *viz.*, V_o , a_o , W_s , R_s and a_s . Subsequently, changing the real radius in steps, same search was repeated again to obtain the best fit parameters with minimum χ^2 value. The final set of best fit parameters for 26 MeV corresponding to minimum χ^2/N value are given in Table 1. For the other incident energies

the same search procedure was followed with the best fit parameters of 26 MeV as the starting parameter set. It is to emphasized that the resultant geometry parameters along with the strengths of the potential components are found to be energy dependent. For instance, the radius values of both the real and imaginary components increases with decreasing energy. The best fit parameters, the minimum χ^2/N values and the corresponding reaction cross sections σ_{reac} have been given in Table 1. The fits are shown by solid lines in Fig.1.

To probe the real and imaginary potentials as a function of energy in the vicinity of the barrier, it is important to identify the radial region of sensitivity of the potentials [25,26,27,28], *i.e.* the region where the potentials are best determined by the elastic scattering data. In order to find the radius of sensitivity or the *crossing radius*, we adopted the procedure described in Ref.[29]. At each energy, we changed the diffuseness parameter a in small steps around the best fit value and adjusted the strength and radius values of the potential to fit the angular distribution data. The process resulted into a family of 'good' potentials having $\chi^2 = \chi^2_{min} + 1$. Almost equivalent reproduction of the angular distribution and the crossing of the potentials at a certain radius value, the *crossing radius*, ensure that the crossing point gives the value of the sensitive radius. Same procedure was adopted to obtain both the real and the imaginary sensitive radial region. Both the real and imaginary sensitive radii were found to be energy dependent. The crossing radius moved to lower radius value as the incident energy was increased. The average value of the crossing radius was estimated to be 9.8 ± 0.4 fm. The strengths of the potential components were determined at this radius to obtain the energy dependent behaviour of the potentials. In Fig.2, the values at the chosen radius of the potentials with Woods Saxon form are shown with solid circles. The error bar with each point includes the distribution in the values of the different 'good' potentials at the chosen radius as well as the errors due to the uncertainty associated with the sensitive radius value itself.

3.2 OM analysis of ${}^6\text{Li}+{}^{64,58}\text{Ni}$ data with folded potential

Following the analysis of the ${}^6\text{Li}+{}^{64}\text{Ni}$ data with the phenomenological Woods Saxon potential, a further analysis of the new data of ${}^6\text{Li}+{}^{64}\text{Ni}$ and the existing data of ${}^6\text{Li}+{}^{58}\text{Ni}$ [22] were performed with folded M3Y potential. Alongwith the real folded potential, two different imagianry model potentials were used. In the first one (OMP1) the model potential had the form

$$U_{OM}(R) = \lambda_r V_f(R) + i\lambda_i V_f(R). \quad (2)$$

where V_f is the folded M3Y potential with unit normalization. λ_r and λ_i are the renormalization factors for real and imaginary components. With geometries fixed, search was performed on these two strength parameters simultaneously to fit the angular distributions.

The second model potential (OMP2) was of *hybrid* nature with the double-folded real potential and the phenomenological imaginary potential

$$U_{OM}(R) = \lambda_r V_f(R) + iW_v(R; W_o, r_w, a_w) \quad (3)$$

where W_v is the imaginary potential of volume Woods-Saxon type. The OMP2 with fixed geometry real part, therefore, has four parameters, *viz.* λ_r , W_o , r_w , a_w to vary to fit the experimental angular distributions.

The double-folded real potentials were generated using the density dependent M3Y-Reid nucleon-nucleon interaction with zero-range exchange term [30]. The density dependence was included following the DDM3Y convention [31] as

$$F(\rho) = C[1 + \alpha \exp(-\beta\rho)] \quad (4)$$

with the parameters C , α and β having the values 0.2845, 3.6391 and 2.9605 $f m^3$ respectively. A linear energy dependent part $g(E)=(1-0.002E)$ had been considered [30] to account for explicit energy dependence of the effective interaction. The mass densities of ^{58}Ni and ^{64}Ni were obtained from Ref.[32]. A parametric form for ^6Li charge density [8] was unfolded for finite proton distribution to obtain the point proton distribution. The neutron distribution was assumed to have the same radial shape for $N=Z$ ^6Li nucleus.

With the model potential OMP1, the two free parameters λ_r and λ_i were varied simultaneously to optimize the fits to the data at all the energies. The best fit values of λ_r and λ_i are given in Table 2 and the corresponding fits are shown by dotted lines in Figs.1 and 3 for $^6\text{Li}+^{64}\text{Ni}$ and $^6\text{Li}+^{58}\text{Ni}$ respectively. The same condition, as described in the case of phenomenological potential, was used to determine the error limits in the values of the individual renormalization factors. To obtain the best fit parameters of the OMP2 potentials for both the isotopes, analysis was started with the highest energy data. At the highest energy, we performed an initial search over all the four parameters simultaneously. Subsequently, the imaginary radius parameter obtained from the initial search was kept fixed. The best fit, determined by χ^2 minimization, was found by searching over the real renormalization factor and the imaginary strength while gridding over the imaginary diffuseness a_w . Same search procedure was adopted for all the incident energies. The radius parameter was held fixed throughout assuming that the change in the value of r_w due to change

in incident energy is not so significant. The best fit parameters along with the χ^2/N (N denotes the number of data points) values and the reaction cross sections $\sigma_{reac.}$ have been given in Table 2. The errors associated with the strength parameters and the reaction cross sections were estimated in the same way as described earlier. The best fit predictions with OMP2 for ${}^6\text{Li}+{}^{64}\text{Ni}$ are shown in Fig.1 by dashed-dotted line and for ${}^6\text{Li}+{}^{58}\text{Ni}$ are shown by solid lines in Fig.3.

In order to find the radius of sensitivity or the *crossing radius* with potential OMP2, we searched over λ_r and W_0 at different diffuseness parameter a_w , obtained by changing its value in small steps while keeping the radius fixed. The χ^2 minimization process yielded different sets of parameter values for OMP2 producing almost equivalent fits to the data. The χ_{min}^2 value for each set of parameters lies within the range of $\chi_{min}^2 \pm \chi_{min}^2/N$ corresponding to the set of best fit parameters. In Fig.4 the crossing points at 14 MeV laboratory energy for ${}^6\text{Li}+{}^{58}\text{Ni}$ and ${}^6\text{Li}+{}^{64}\text{Ni}$ systems have been compared. It is to be noted that with OMP2 we have obtained the sensitive radius of the imaginary potential only. The observed crossing points are quite sharp for ${}^6\text{Li}+{}^{64}\text{Ni}$ but for ${}^6\text{Li}+{}^{58}\text{Ni}$ the crossing points are not so unambiguous at certain energies. The radii of sensitivity for imaginary potentials found from the analyses of the data vary with the incident energy. The value increases by $\sim 25\%$ at the lowest energy studied. At the higher incident energies the values of the crossing radii are close to the strong absorption radii, R_{sa} , of the systems.

Considering the energy variation of the crossing radius and the uncertainty associated with it, we have used in the dispersion relation the integral quantities $G_x(E)$ defined as

$$G_x(E) = \frac{4\pi}{A_P A_T} \int x(R, E) G(R) R^2 dR \quad (5)$$

where $G(R)$ is the Gaussian weighting function centered on some average value of the crossing radii and x denoting either the real potential $V(R,E)$ or the imaginary potential $W(R,E)$ for the respective integral quantity. It was demonstrated that the dispersion relation can be extended to the integral quantities with Gaussian weighting function [10,33], such that

$$G_V(E) = G_{V_o}(E) + \Delta G_V(E) \quad (6)$$

where

$$\Delta G_V(E) = \frac{P}{\pi} \int \frac{G_W(E')}{E' - E} dE' \quad (7)$$

The Gaussian weighting function has the usual form of

$$G(R) = \frac{1}{\sqrt{2\pi}\sigma_G} \exp\left[-\frac{(R - R_G)^2}{2\sigma_G^2}\right] \quad (8)$$

The choices of radius parameter R_G and the width parameter σ_G of the Gaussian weighting function are very crucial for systems involving light, loosely bound projectiles. Although the regions of sensitivity are narrow at each energy, the crossing radii vary with energy. To identify the suitable values of R_G and σ_G , we estimated the uncertainties associated with the integral quantities with different combinations of (R_G, σ_G) . It can easily be understood that the range of uncertainties associated with $G_V(E)$ and $G_W(E)$ at a particular energy changes significantly depending upon the proximity of the chosen R_G to crossing radius at that energy. So the final choice of R_G and σ_G is a compromise relative to the uncertainties associated with $G_V(E)$ and $G_W(E)$ at each energy. The chosen value of R_G is 9.8fm for both ^{64}Ni and ^{58}Ni targets. The associated σ_G was chosen to be 0.6fm. We would like to emphasize that the choice of R_G does not really change the overall trend of the energy variations of $G_V(E)$ and $G_W(E)$. The quantities $G_V(E)$ and $G_W(E)$ as functions of incident energy for ^{64}Ni and ^{58}Ni are shown in Figs.5 and 6. The error bars shown in the figures predominantly arise out of the variations in the values of the *good potentials* at R_G within the width defined by σ_G . In Fig.7, we have shown the best fit normalizations λ_r and λ_i , obtained with model potential OMP1, as a function of energy for $^6\text{Li}+^{58,64}\text{Ni}$. Errors shown are estimated individually for each parameter using the condition of Eq.4. The plotting of these normalization factors directly is justified considering the fact that dispersion relation involving these factors will not depend on the choice of the radial point for the evaluation of the energy integration.

4 Results and Discussion

The phenomenological analysis of $^6\text{Li}+^{64}\text{Ni}$ data with Woods Saxon potential having variable geometry with decreasing energy yielded an energy dependence of the surface strengths of the real and imaginary components shown in Fig.2. The variations resulted from the model potentials OMP1, with fixed geometry real and imaginary components, and OMP2, with fixed geometry real and variable geometry imaginary components, are also shown in Fig.2. Good matching in the surface strengths of the imaginary potential at all the energies have been obtained for the three different model potentials used in the analysis. The magnitude of the real strength, however, shows some kind of model dependence. Despite the difference in the magnitudes, the three model potentials exhibit similar trend in the energy variation of the real strength.

The observed variation indicates that the strength of the imaginary potential increases initially as the ${}^6\text{Li}$ projectile energy approaches the barrier for the system. With further decrease of incident energy the strength of the imaginary potential starts to decrease. On the otherhand, the real strength shows an overall increase with decreasing energy although there is a tendency to decline around 18 MeV energy. This feature is more prominent in the case of phenomenological potential with variable geometry.

The observed variations of $G_W(E)$ in Figs.5 and 6 also indicate the same behaviour for the strengths of the imaginary and the real potentials for both the Ni isotopes as the ${}^6\text{Li}$ projectile energy approaches the barrier for the systems. In order to find the connectivity between the energy dependence of the real and imaginary components through the dispersion relation, we fitted the observed variation of $G_W(E)$ with the following functional form

$$\begin{aligned}
G_W(E) &= 0 & , E \leq E_1 \\
&= C_1(E - E_1) & , E_1 \leq E \leq E_2 \\
&= C_1(E_2 - E_1) + C_2(E - E_2) & , E_2 \leq E \leq E_3 \\
&= C_3 & , E \geq E_3
\end{aligned} \tag{9}$$

With this three linear segments form of energy dependence for $G_W(E)$, the dynamical contribution to the real part, *i.e.* the real polarization component is given by

$$\begin{aligned}
\Delta G_V(E) &= \frac{1}{\pi} [(G_W(E_1) - G_W(E_2))(\epsilon_1 \ln|\epsilon_1| - \epsilon_2 \ln|\epsilon_2|) \\
&\quad + (G_W(E_2) - G_W(E_3))(\epsilon'_2 \ln|\epsilon'_2| - \epsilon'_3 \ln|\epsilon'_3|)]
\end{aligned} \tag{10}$$

where $\epsilon_i = (E - E_i)/(E_2 - E_1)$ and $\epsilon'_i = (E - E_i)/(E_3 - E_2)$. The energy E_1 is the threshold energy where the absorption goes to zero. It has been determined assuming that the function ($\sqrt{E\sigma_{\text{reac.}}}$) behaves as a linear function of energy E in the sub-barrier region [34]. E_2 is the energy at which the increasing and the decreasing linear segments intersect while E_3 is the energy beyond which the variation of $G_W(E)$ or rather the imaginary potential $W(E)$ is assumed to be independent of energy. The values of the coefficients C_i and energies E_i for both the systems are given in Table 2. The solid curves in the plots of $G_V(E)$ vs. E in Figs.5 & 6 indicate the dispersion relation prediction following Eq.10. The general agreement with the observed trend in $G_V(E)$ is quite good considering the simple form employed to describe $G_W(E)$.

As it appears from Figs.5 and 6, the imaginary potential, for both ${}^6\text{Li}+{}^{58}\text{Ni}$ and ${}^6\text{Li}+{}^{64}\text{Ni}$, shows a distinct increasing trend as the energy approaches the

barrier but with further lowering of energy below the barrier it starts to decrease. The interplay of the dispersive contributions of these two regions in $W(E)$ constitute the effective energy dependence of the real potential. The resultant energy dependence of the real polarization potential exhibits an overall increasing trend. This suggests to the presence of *threshold anomaly* (TA) for ${}^6\text{Li}$ scattering from medium mass Ni isotopes. However, a careful inspection also reveals that as the bombarding energy decreases and approaches the barrier, the strength of the real effective potential increases slowly at the beginning and then shows a weak declining trend around 1.2 times the barrier before sharply rising again. This decreasing tendency of the real potential is associated with the increasing part of the imaginary potential. Similar behaviour for the real and imaginary components of the effective potential has also been observed for ${}^6\text{Li}+{}^{208}\text{Pb}$ [12], ${}^6\text{Li}+{}^{59}\text{Co}$ [35,20] and ${}^6\text{Li}+{}^{27}\text{Al}$ [36,37] systems and has been termed as *breakup threshold anomaly* or BTA. For ${}^6\text{Li}+{}^{208}\text{Pb}$ [12], the strength of the real effective potential continues to decrease even below the barrier indicating the presence of reaction channels, like break up, producing strong repulsive real polarization even at sub barrier energies. However, our investigation of ${}^6\text{Li}$ scattering from medium mass Ni-isotopes suggests that the observed threshold anomaly has the usual form albeit modified by coupling to breakup (or channels producing repulsive real polarization). A recent two-body continuum discretized coupled channel (CDCC) calculation [35] for ${}^6\text{Li}$ on ${}^{59}\text{Co}$ has shown that the real potential does exhibit an overall increasing trend while the imaginary potential falls off after a short increase near the barrier. It is, therefore, extremely important to investigate the target mass dependence of *threshold anomaly* for projectiles with low breakup threshold, as has been pointed out by Beck, *et al.* [35], in order to understand the evolution of breakup coupling with increasing or decreasing mass at near barrier energies.

In Fig.7a) & b) we have compared the observed energy dependence of the renormalization parameters λ_r and λ_i obtained by fitting the elastic angular distributions of ${}^6\text{Li}+{}^{58,64}\text{Ni}$ with potential OMP1. It is to be noted that the variation of the renormalization parameters is independent of the choice of interaction distance. For both the systems the variations in λ_r and λ_i with incident energy are very similar to the variations observed in the integral quantities $G_V(E)$ and $G_W(E)$. The observed energy dependence of λ_r and λ_i for ${}^6\text{Li}+{}^{58}\text{Ni}$ and ${}^6\text{Li}+{}^{64}\text{Ni}$ in Fig.7 does not indicate of any dramatic isotopic variation. However, careful observation will show that the rise in the imaginary strength for the ${}^6\text{Li}+{}^{64}\text{Ni}$ system starts earlier than the ${}^6\text{Li}+{}^{58}\text{Ni}$ system. This is also obvious from the values of E_2 parameter in Table 2. The fall off in the imaginary strength around the barrier is slower in the case of lighter Ni isotope but the large error bars in the lowest energies do not allow the observation to be conclusive. Exclusive coincident measurement of fragments produced in break up or transfer followed by break up reactions at these bombarding energies can throw some light on the possible difference in the observed behaviour.

5 Summary

In this work the elastic scattering angular distributions measured in the bombarding energy range $13 \text{ MeV} \leq E_{lab} \leq 26 \text{ MeV}$ around the Coulomb barrier for the system ${}^6\text{Li}+{}^{64}\text{Ni}$ have been presented. The measured elastic scattering data for ${}^6\text{Li}+{}^{64}\text{Ni}$ has been investigated with three different model potentials - a phenomenological Woods Saxon potential with variable geometry as energy changes, a fixed geometry folded DDM3Y potential with complex renormalization factor and a *hybrid* potential with fixed geometry real folded potential and variable geometry phenomenological imaginary potential. The existing data for the ${}^6\text{Li}+{}^{58}\text{Ni}$ system have, subsequently, been analyzed using the folded DDM3Y potential with complex normalization and also the hybrid potential model. The fitting procedure yielded the energy dependence of the real and imaginary components - the data required to demonstrate the existence or non-existence of the threshold anomaly for ${}^6\text{Li}+{}^{58}\text{Ni}$ and ${}^6\text{Li}+{}^{64}\text{Ni}$ systems.

The near threshold behaviour of all the model interaction potentials are similar in nature for both the systems. The imaginary potential falls off after a short increasing region close to the barrier. On the otherhand, the real potential shows an overall increasing trend with decreasing energy. But there is definite tendency to decline in the energy region where the imaginary potential shows an increasing nature. The observed energy dependences of the real and imaginary potentials corroborate with the observations from the study of ${}^6\text{Li}+{}^{59}\text{Co}$ and ${}^6\text{Li}+{}^{27}\text{Al}$ systems. This particular nature of the interaction potential close to the barrier has been argued to be due to the coupling to the continuum. However, unlike the ${}^6\text{Li}+{}^{208}\text{Pb}$ system, the real potential instead of decreasing further in the sub-barrier energy region shows a sharp rise. A dispersion relation prediction for the real potential behaviour assuming a simple 3-linear segment description of the energy dependence of the imaginary potential describes nicely the observed energy variation of the real component. In order to pinpoint the threshold behaviour of the interaction potential with loosely bound projectiles, further experimental investigations with more precision and in smaller energy steps around the barrier is necessary. Also a complete CRC calculation including the coupling to the inelastic and other direct reaction channels in the presence of coupling to the continuum is necessary to understand the observed energy variations of the real and imaginary potentials for ${}^6\text{Li}+{}^{58}\text{Ni}$ and ${}^6\text{Li}+{}^{64}\text{Ni}$ systems.

Table 1

Best fit parameters with phenomenological potential (PH) for ${}^6\text{Li}+{}^{64}\text{Ni}$

$E_{lab}(\text{MeV})$	V_0	R_0	a_0	W_s	R_s	a_s	χ^2/N	$\sigma_R(\text{mb})$
13.0	34.1	6.736	0.737	5.107	7.196	0.703	0.13	196.5
14.0	24.4	6.457	0.760	4.081	7.196	0.812	0.54	388.4
17.0	38.1	5.978	0.743	3.18	7.218	0.838	0.40	813.1
19.0	36.8	5.936	0.755	3.743	6.944	0.844	0.45	983.2
26.0	46.0	5.860	0.757	7.73	6.000	0.944	0.45	1538.9

6 Acknowledgments

The authors thank the BARC/TIFR Pelletron staff for delivering the ${}^6\text{Li}$ beam. Thanks are also due to Mr. Pradipta Das and Mr. B.P. Das for their help in preparing the targets. We also thank Mr. Ajay K. Mitra for his extensive support during the experiment.

References

- [1] N. Keeley, et al., Nucl.Phys. A 571 (1994) 326
- [2] C. Signorini, et al., Phys. Rev. C 61 (2000) 061603(R)
- [3] W.Y. So, S.W. Hong, B.T. Kim and T. Udagawa, Phys. Rev. C 69 (2004) 064606
- [4] J.M. Figueira, et al., Phys. Rev. C 73 (2006) 054603
- [5] A. Gomez Camacho, E.F. Aguilera, A.M. Moro, Nucl. Phys. A 762 (2005) 216
- [6] S.B. Moraes, et al., Phys. Rev. C 61 (2000) 064608
- [7] A. Pakou, et al., Phys. Lett. B 556 (2003) 21
- [8] G.R. Satchler and W.G. Love, Phys. Rep. 55 (1979) 183
- [9] G.R. Satchler, Phys. Rep. 199 (1991) 147
- [10] C. Mahaux, H. Ngo and G.R. Satchler, Nucl. Phys. A 449 (1986) 354.
- [11] Y. Sakuragi, Phys. Rev. C 35 (1987) 2161
- [12] M.S. Hussein, P.R.S. Gomes, J. Lubian and L.C. Chamon, Phys. Rev. C 73 (2006) 044610
- [13] D.J. Hinde, et al., Phys. Rev. Lett 89 (2002) 272701
- [14] E.F. Aguilera, et al., Phys. Rev. C 63 (2001) 061603(R)

Table 2
Best fit potential parameters with folded potential

$E_{lab}(\text{MeV})$	Model	λ_r	λ_i	W_0	R_w	a_w	χ^2/N	$\sigma_R(\text{mb})$
For ${}^6\text{Li}+{}^{64}\text{Ni}$								
13.0	OMP1	0.88 ± 0.21	0.91 ± 0.3				0.13	196.0 ± 29.0
	OMP2	0.93 ± 0.11		52.01 ± 18.00	6.753	0.665	0.13	197.8 ± 10.8
14.0	OMP1	0.75 ± 0.05	1.240 ± 0.11				0.52	372.25 ± 11.6
	OMP2	0.75 ± 0.04		41.13 ± 3.67	6.753	0.724	0.58	369.9 ± 11.7
17.0	OMP1	0.69 ± 0.02	0.88 ± 0.02				0.43	765.8 ± 6.0
	OMP2	0.60 ± 0.02		31.92 ± 1.60	6.753	0.744	0.40	778.3 ± 9.1
19.0	OMP1	0.60 ± 0.02	0.72 ± 0.05				0.54	945.7 ± 9.8
	OMP2	0.51 ± 0.02		23.56 ± 3.70	6.753	0.764	0.53	953.4 ± 15.2
26.0	OMP1	0.63 ± 0.04	0.61 ± 0.04				0.47	1407.8 ± 20.57
	OMP2	0.60 ± 0.06		23.87 ± 2.93	6.753	0.766	0.53	1460.3 ± 38.8
For ${}^6\text{Li}+{}^{58}\text{Ni}$								
12.0	OMP1	0.99 ± 0.09	0.90 ± 0.13				0.11	52.5 ± 5.1
	OMP2	1.15 ± 0.21		97.84 ± 41.00	6.598	0.585	0.11	51.9 ± 12.0
14.0	OMP1	0.68 ± 0.02	1.09 ± 0.06				0.18	269.5 ± 6.0
	OMP2	0.81 ± 0.03		70.85 ± 11.01	6.598	0.633	0.18	266.3 ± 14.4
16.0	OMP1	0.64 ± 0.02	0.90 ± 0.02				0.51	528.6 ± 1.5
	OMP2	0.66 ± 0.02		39.53 ± 4.48	6.598	0.686	0.52	526.7 ± 15.3
18.0	OMP1	0.55 ± 0.004	0.63 ± 0.01				0.25	709.7 ± 2.2
	OMP2	0.42 ± 0.014		18.77 ± 2370	6.598	0.795	0.23	746.4 ± 24.3
20.0	OMP2	0.57 ± 0.01	0.69 ± 0.02				1.5	922.5 ± 0.2
	OMP2	0.45 ± 0.02		22.12 ± 1.70	6.598	0.797	0.94	980.6 ± 17.6

Table 3
Parameters of 3-linear segment fit of $G(E)_W$

$E_1(\text{MeV})$	$E_2(\text{MeV})$	$E_3(\text{MeV})$	C_1	C_2	C_3
For ${}^6\text{Li}+{}^{64}\text{Ni}$					
9.56	13.49	19.0	0.639	-0.156	1.62
For ${}^6\text{Li}+{}^{58}\text{Ni}$					
10.03	12.25	17.78	1.09	-0.192	1.36

- [15] Y.W. Wu, et al., Phys. Rev. C 68 (2003) 044605
- [16] R.J. Woolliscroft, et al., Phys. Rev. C 68 (2003) 014611
- [17] W.Y. So, T. Udagawa, K.S. Kim, S.W. Hong and B.T. Kim, Phys. Rev. C 75 (2007) 024610
- [18] I. Martel, et al., Nucl.Phys. A 582 (1995) 357
- [19] A. Pakou, et al., Phys. Rev. C 69 (2004) 054602
- [20] F.A. Souza, et al., Phys. Rev C 75 (2007) 044601
- [21] N. Keeley, et.al., Nucl. Phys. A 582 (1995) 314
- [22] K.O. Pfeiffer, E. Speth and K. Bethge, Nucl. Phys. A 206 (1973) 545
- [23] LAMPS: Linux Advanced Multiparameter System; A. Chatterjee (private communication); www.tifr.res.in/~pell/lamps.html
- [24] J. Raynal, *ECIS94*, NEA 0850/16
- [25] M.E. Brandan, Phys. Rev. C 58 (1993) 1147
- [26] C. Tenreiro, et al., Phys. Rev. C 53 (1996) 2870
- [27] A. Pakou and K. Rusek, Phys. Rev. C 69 (2004) 057602
- [28] D. Roubos, A. Pakou, N. Alamanos and K. Rusek, Phys. Rev. C 73 (2006) 051603(R)
- [29] H. Wojciechowski, et al., Phys. Rev. C 17 (1978) 2126
- [30] Dao T. Khoa and W. von Oertzen, Phys.Lett. B 304 (1993) 8; Dao T. Khoa, W. von Oertzen and H.G. Bohlen, Phys. Rev. C 49 (1994) 1652
- [31] A.M. Kobos, B.A. Brown, P.E. Hodgson, G.R. Satchler and A. Budzanowski, Nucl. Phys. A 384 (1982) 65
- [32] <http://www-nds.iaea.org/ripl-2>
- [33] C. Mahaux, H. Ngo and G.R. Satchler, Nucl. Phys. A 456 (1986) 134.
- [34] P.H. Stelson, Phys. Lett. B 205 (1988) 190; P.H. Stelson, et al., Phys. Rev. C 41 (1990) 1584
- [35] C. Beck, N.Keeley and A. Diaz-Torres, Phys. Rev C 75 (2007) 054605
- [36] J.O. Fernández Niello, et al., Nucl. Phys. A 787 (2007) 484c
- [37] J.M. Figueira, et al., Phys. Rev C 75 (2007) 017602
- [38] R.A. Broglia and A. Winther, Heavy Ion Reactions, Vol. I: Elastic and Inelastic Reactions, Benjamin-Cummings Publishing Company, 1981.

FIGURE CAPTIONS

- Fig. 1. Elastic angular distributions of ${}^6\text{Li}+{}^{64}\text{Ni}$. The solid line represents prediction with the phenomenological potential. The dashed-dotted (dotted) curves are the predictions using the model potential OMP2 (OMP1).
- Fig. 2. The energy dependence of the real and imaginary surface strengths at an average radius of 9.8 fm obtained with the phenomenological (solid circle), OMP1 (open circle) and OMP2 (solid triangle) model potentials for ${}^6\text{Li}+{}^{64}\text{Ni}$ system.
- Fig. 3. Elastic angular distributions of ${}^6\text{Li}+{}^{58}\text{Ni}$. The solid (dotted) line represents prediction of OMP2 (OMP1).
- Fig. 4. Crossing points of 'good' imaginary potentials (OMP2) at 14 MeV for ${}^6\text{Li}+{}^{58}\text{Ni}$ and ${}^6\text{Li}+{}^{64}\text{Ni}$ systems.
- Fig. 5. Energy variations of Gauss weighted integral quantities of real and imaginary components of OMP2 for ${}^6\text{Li}+{}^{64}\text{Ni}$. The solid line in the upper panel is the dispersion relation prediction with 3-linear segment fit of the imaginary component. The dotted line in the upper panel depicts the intrinsic energy dependence of the Gauss weighted integral of unrenormalized real part of OMP2. $E_{C.b.}=13.8$ MeV is the value of the Coulomb barrier for ${}^6\text{Li}+{}^{64}\text{Ni}$ system in the laboratory [38]
- Fig. 6. Energy variations of Gauss weighted integral quantities of real and imaginary components of OMP2 for ${}^6\text{Li}+{}^{58}\text{Ni}$. The solid line in the upper panel is the dispersion relation prediction with 3-linear segment fit of the imaginary component. The dotted line in the upper panel depicts the intrinsic energy dependence of the Gauss weighted integral of unrenormalized real part of OMP2. $E_{C.b.}=14.1$ MeV is the value of the Coulomb barrier for ${}^6\text{Li}+{}^{58}\text{Ni}$ system in the laboratory [38]
- Fig. 7. Energy dependence of the effective real and imaginary normalization factors with model potential OMP1. The solid circle corresponds to ${}^6\text{Li}+{}^{64}\text{Ni}$ and the hollow circle to ${}^6\text{Li}+{}^{58}\text{Ni}$. $E_{C.b.}$ for the two systems are specified in the captions of Figs. 5 and 6.

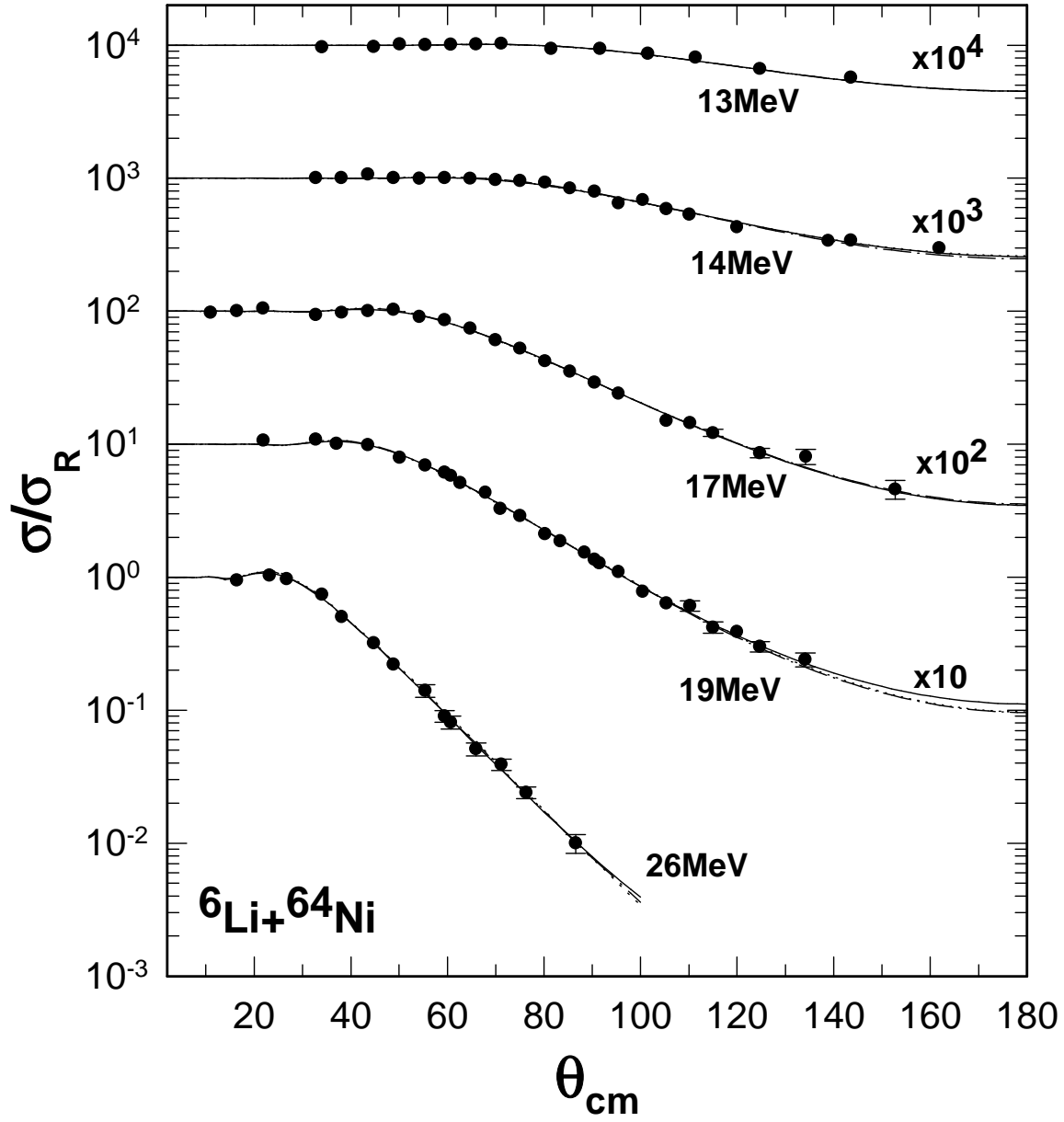


Fig. 1. Elastic angular distributions of $^6\text{Li} + ^{64}\text{Ni}$. The solid line represents prediction with the phenomenological potential. The dashed-dotted (dotted) curves are the predictions using the model potential OMP2 (OMP1).

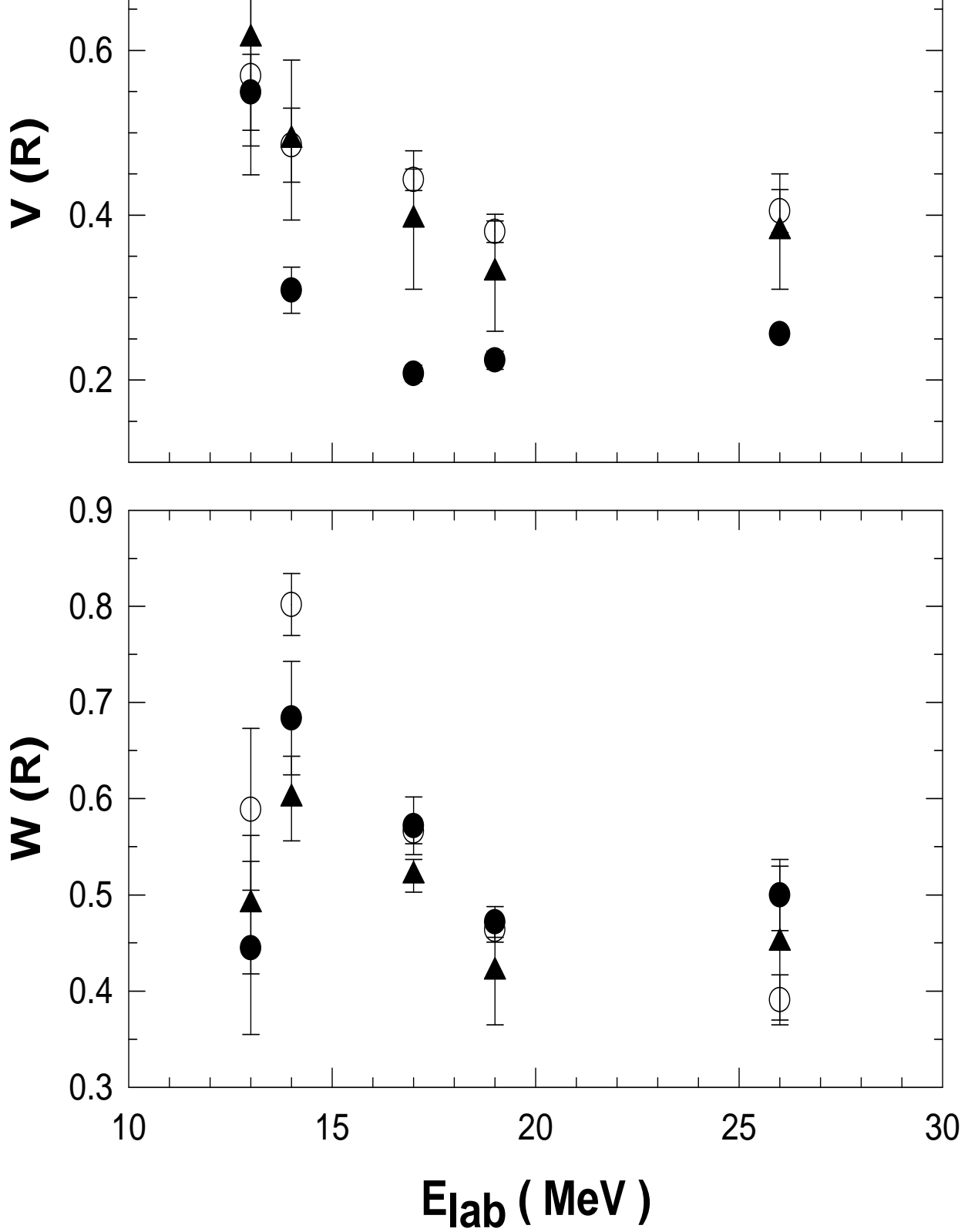


Fig. 2. The energy dependence of the real and imaginary surface strengths at an average radius of 9.8 fm obtained with the phenomenological (solid circle), OMP1 (open circle) and OMP2 (solid triangle) model potentials for ${}^6\text{Li}+{}^{64}\text{Ni}$ system.

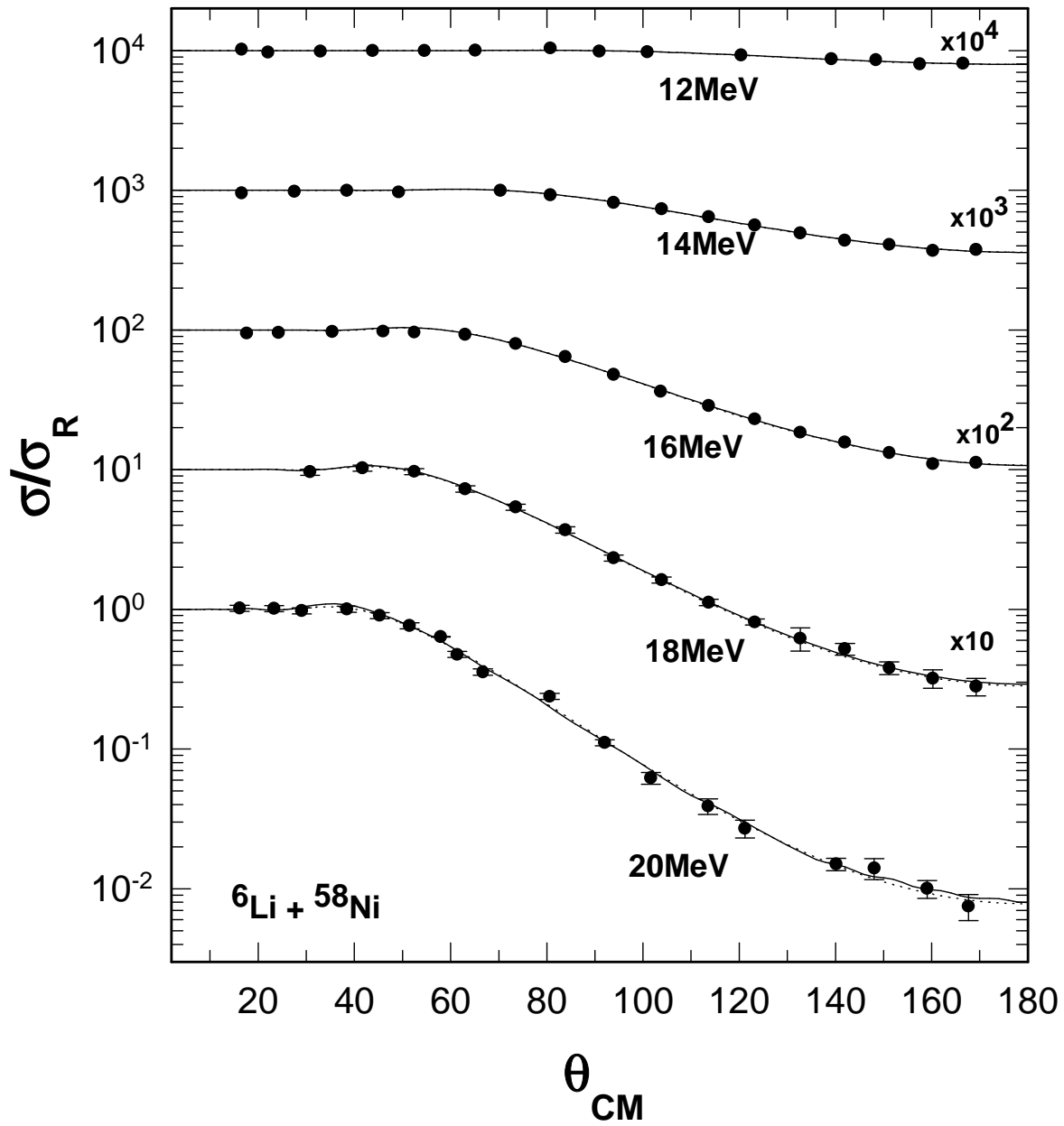


Fig. 3. Elastic angular distributions of $^6\text{Li} + ^{58}\text{Ni}$. the solid (dotted) line represents prediction of OMP2 (OMP1).

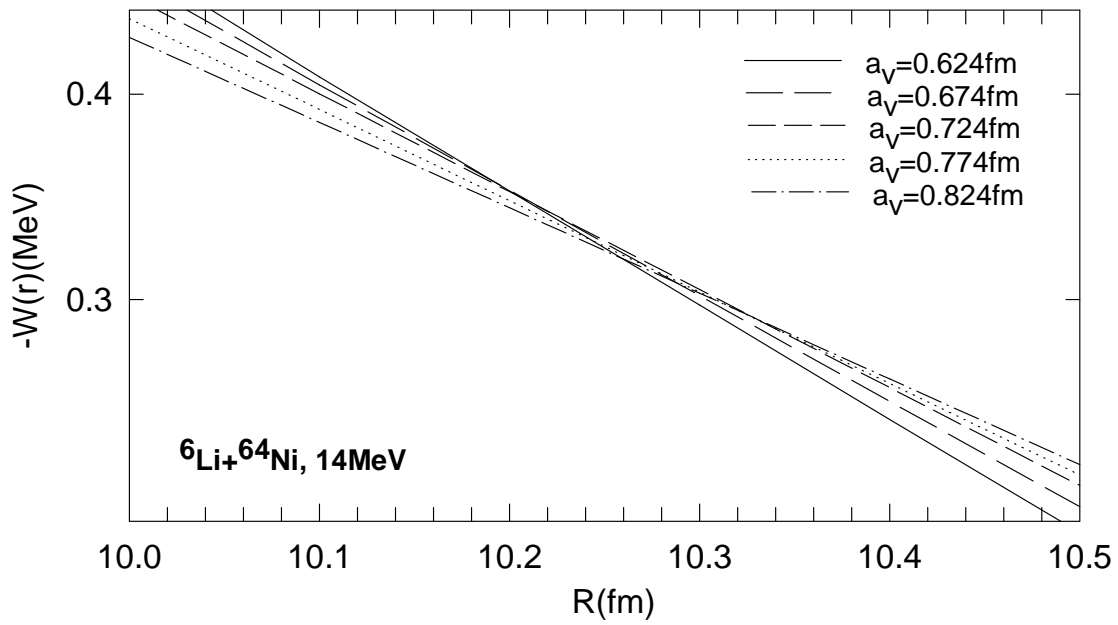
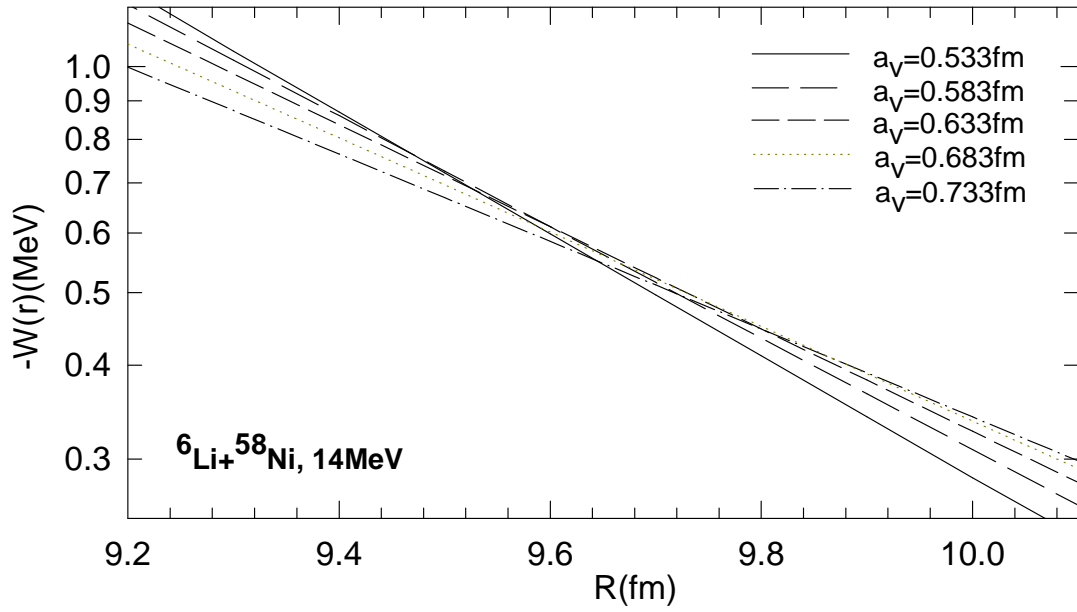


Fig. 4. Crossing points of 'good' imaginary potentials (OMP2) at 14 MeV for ${}^6\text{Li}+{}^{58}\text{Ni}$ and ${}^6\text{Li}+{}^{64}\text{Ni}$ systems.

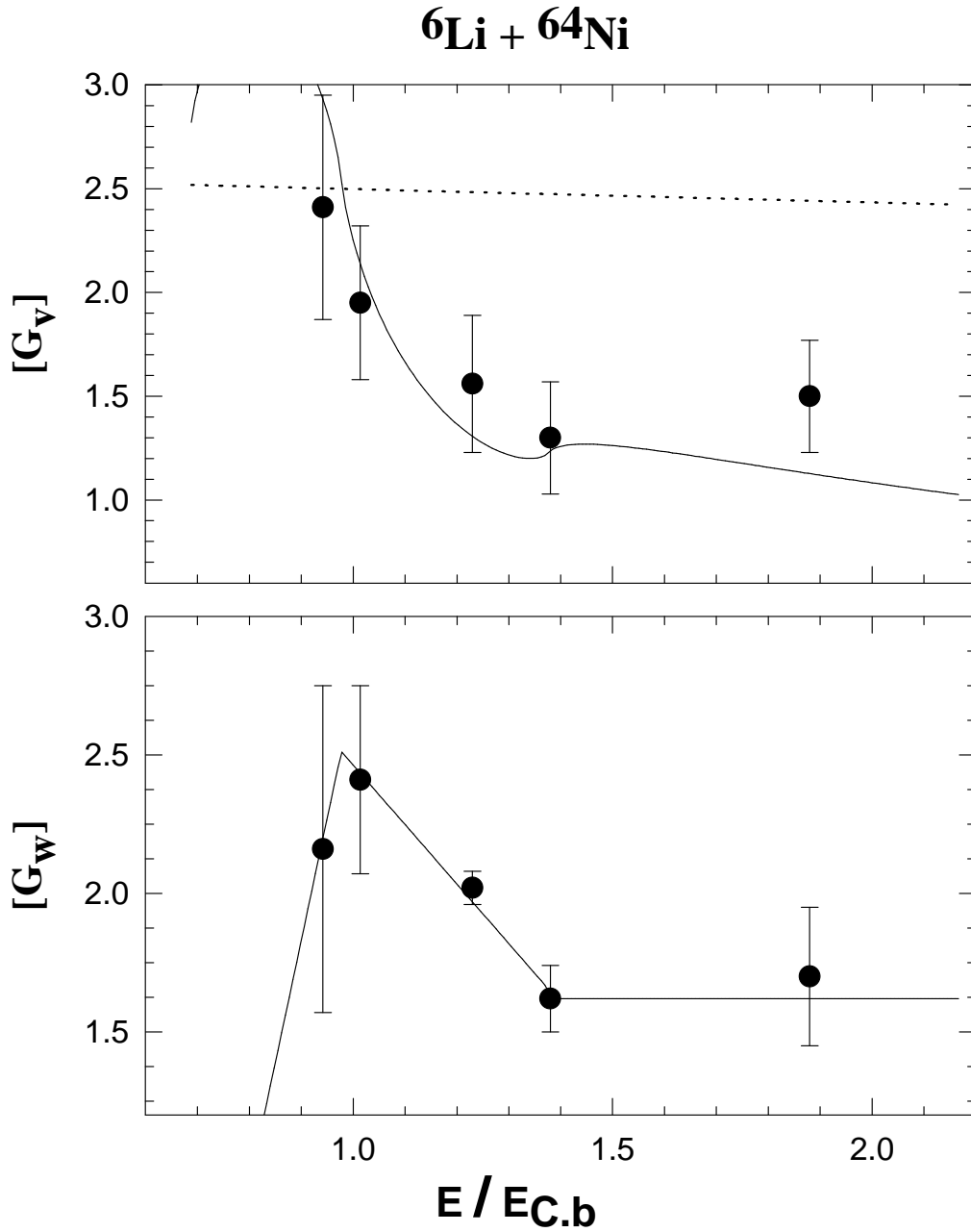


Fig. 5. Energy variations of Gauss weighted integral quantities of real and imaginary components of OMP2 for ${}^6\text{Li}+{}^{64}\text{Ni}$. The solid line in the upper panel is the dispersion relation prediction with 3-linear segment fit of the imaginary component. The dotted line in the upper panel depicts the intrinsic energy dependence of the Gauss weighted integral of unrenormalized real part of OMP2. $E_{C,b}=13.8$ MeV is the value of the Coulomb barrier for ${}^6\text{Li}+{}^{64}\text{Ni}$ system in the laboratory [38]

${}^6\text{Li} + {}^{58}\text{Ni}$

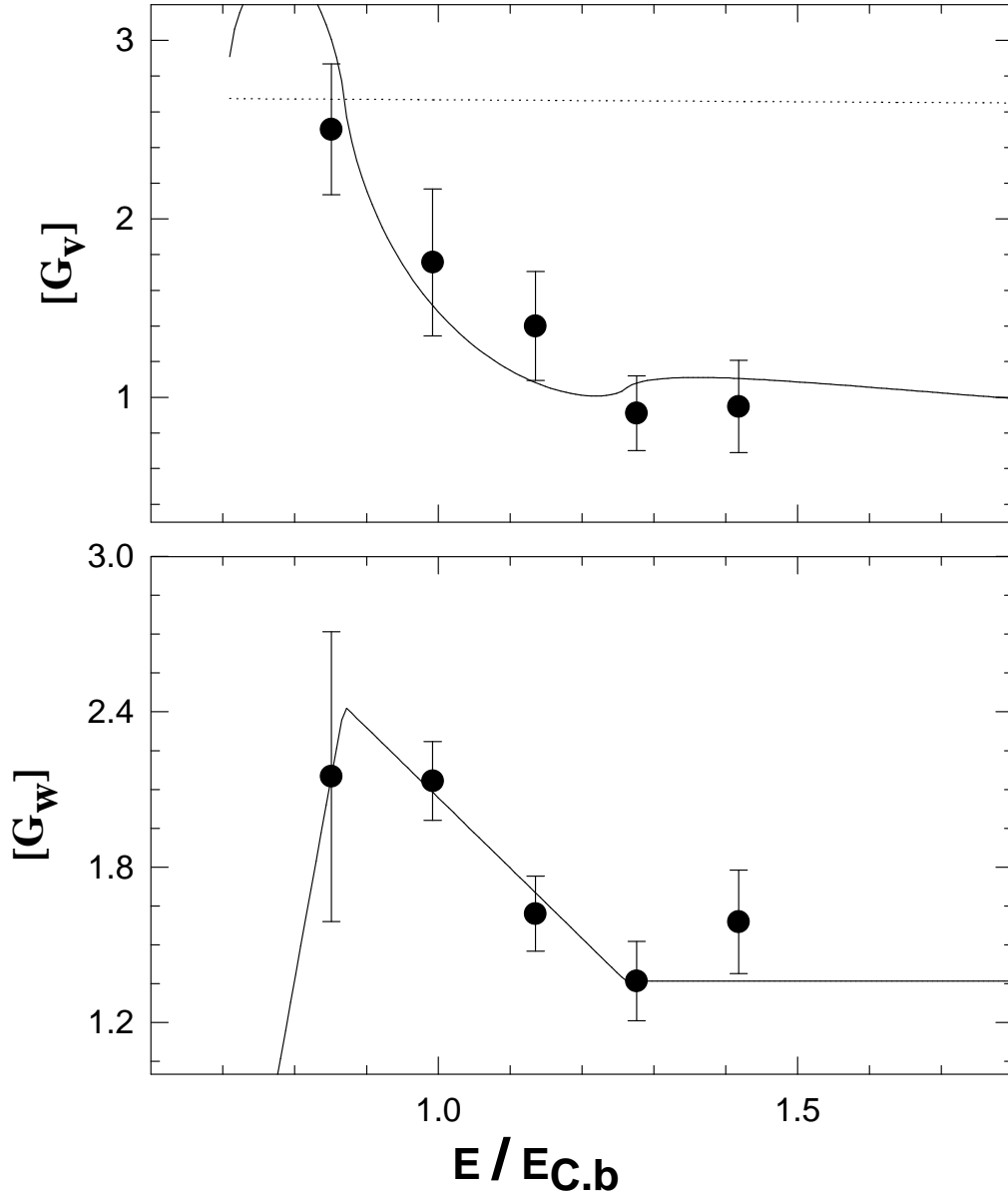


Fig. 6. Energy variations of Gauss weighted integral quantities of real and imaginary components of OMP2 for ${}^6\text{Li}+{}^{58}\text{Ni}$. The solid line in the upper panel is the dispersion relation prediction with 3-linear segment fit of the imaginary component. The dotted line in the upper panel depicts the intrinsic energy dependence of the Gauss weighted integral of unrenormalized real part of OMP2. $E_{C,b}=14.1$ MeV is the value of the Coulomb barrier for ${}^6\text{Li}+{}^{58}\text{Ni}$ system in the laboratory [38]

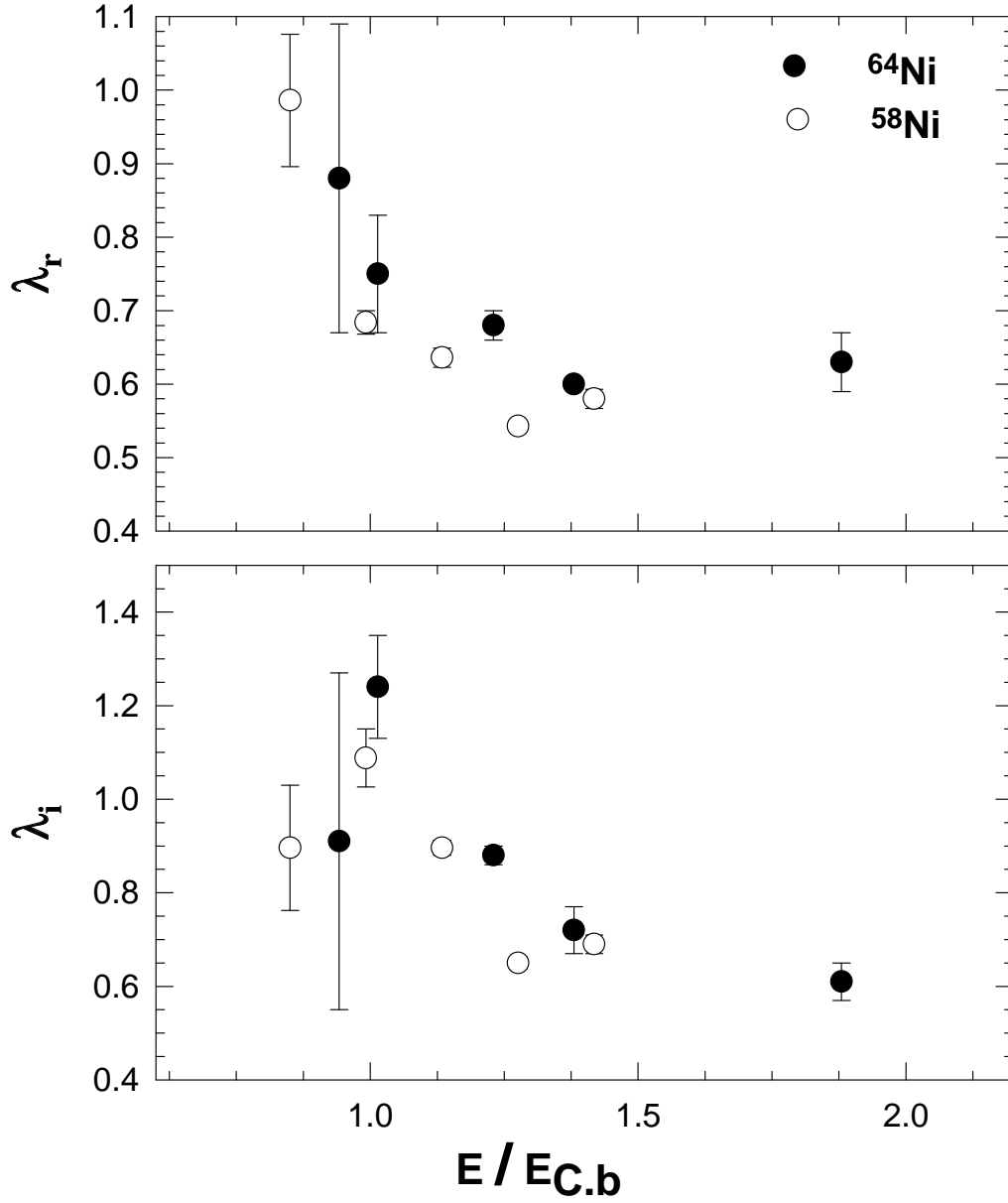


Fig. 7. Energy dependence of the effective real and imaginary normalization factors model potential OMP1. The solid circle corresponds to ${}^6\text{Li}+{}^{64}\text{Ni}$ and the hollow circle to ${}^6\text{Li}+{}^{58}\text{Ni}$. $E_{C.b}$ for the two systems are specified in the captions of Figs. 5 and 6.